

Learning Agile and Robust Omnidirectional Aerial Motion on Overactuated Tilttable-Quadrotors

Wentao Zhang¹ Zhaoqi Ma¹ Jinjie Li¹ Huayi Wang² Haokun Liu¹ Junichiro Sugihara¹
Chen Chen¹ Yicheng Chen¹ Moju Zhao^{1,†}

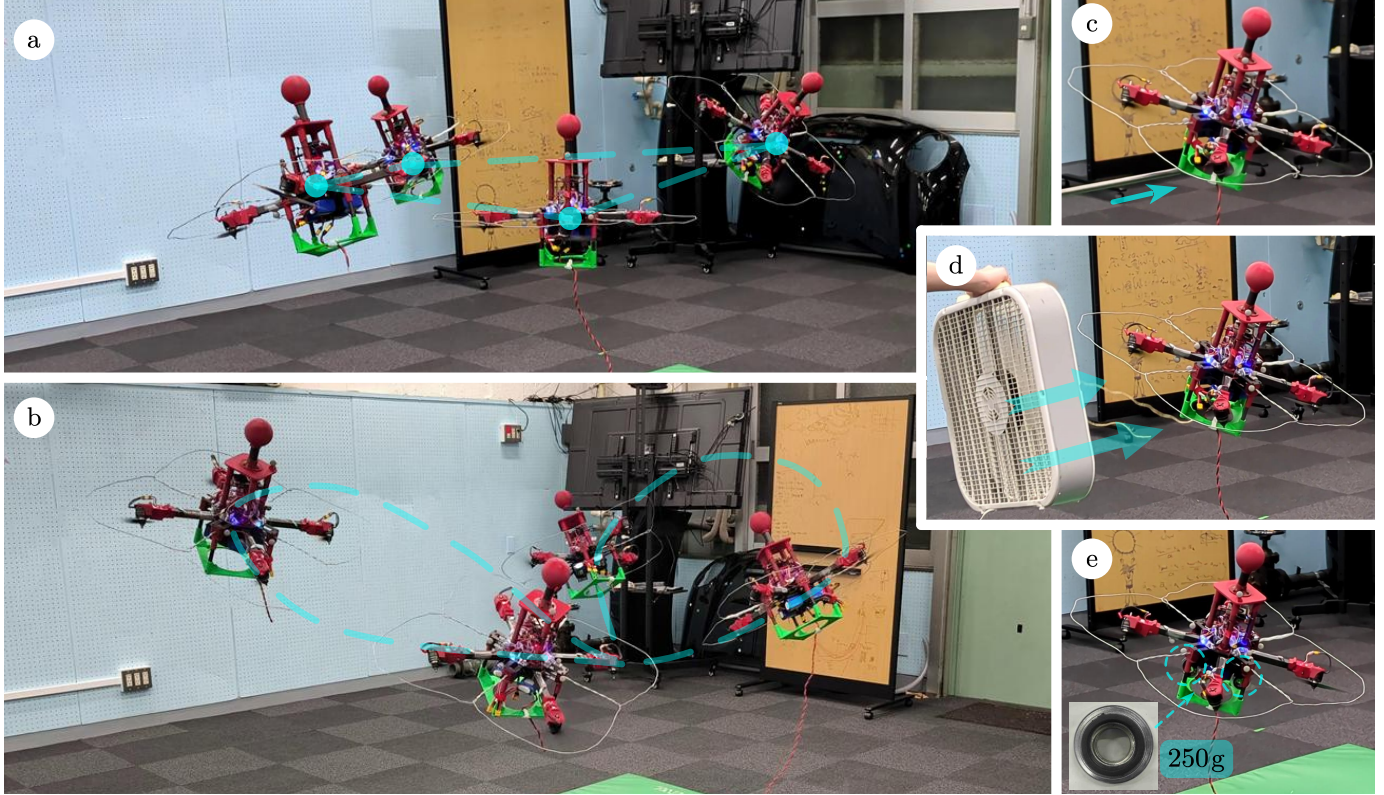


Fig. 1: Proposed RL framework enables agile and robust real-world flight across multiple scenarios. (a) Waypoints hovering, (b) Trajectory tracking, (c) External force recovery, (d) Wind disturbance rejection, and (e) Payload variation ($0.25 \text{ kg} \times 2$).

Abstract—Tilt-rotor aerial robots enable omnidirectional maneuvering through thrust vectoring, but introduce significant control challenges due to the strong coupling between joint and rotor dynamics. While model-based controllers can achieve high motion accuracy under nominal conditions, their robustness and responsiveness often degrade in the presence of disturbances and modeling uncertainties. This work investigates reinforcement learning for omnidirectional aerial motion control on over-actuated tilttable quadrotors that prioritizes robustness and agility. We present a learning-based control framework that enables efficient acquisition of coordinated rotor-joint behaviors for reaching target poses in the $SE(3)$ space. To achieve reliable sim-to-real transfer while preserving motion accuracy, we integrate system identification with minimal and physically consistent domain randomization. Compared with a state-of-the-art NMPC controller, the proposed method achieves comparable six-degree-of-freedom pose tracking accuracy, while demonstrating superior robustness and generalization across diverse tasks, enabling zero-shot deployment on real hardware.

I. INTRODUCTION

Aerial robots have demonstrated remarkable capabilities across a wide range of applications. In particular, quadrotors have been extensively deployed in practice, such as inspection, delivery, and search and rescue [5, 39, 41, 45]. Despite their success, conventional quadrotors are inherently underactuated, limiting their ability to independently control position and orientation, which restricts more advanced aerial interaction and pose-critical tasks. To address these limitations, omnidirectional aerial robots have recently attracted increasing attention, as they enable full six-degree-of-freedom (6D) motion and allow arbitrary pose control in 3D space [20, 7, 18]. Among various designs, tilt-rotor aerial robots stand out for their capability to actively reorient thrust directions and achieve high actuation efficiency [31, 23, 43, 44]. However, this enhanced capability comes at the cost of substantially more complex system dynamics, where strong coupling between rotor and joint dynamics poses significant challenges for motion control.

¹ University of Tokyo, ² Shanghai Jiao Tong University.

Paper website: <https://zwt006.github.io/posts/BeetleOmni/>

Controllers for tilt-rotor aerial robots have traditionally relied on model-based approaches, including Geometric Control [1, 18, 35] and Nonlinear Model Predictive Control (NMPC) [30, 19]. In these approaches, accurate modeling of the robot dynamics is crucial for achieving high-performance motion control. However, constructing sufficiently accurate models remains difficult in practice due to strong coupling between rotor aerodynamics, joint actuation, and floating base motion. As a result, model-based controllers often rely on simplifying assumptions that may limit their effectiveness in practical scenarios. Moreover, their performance is sensitive to modeling errors and external disturbances, requiring extensive parameter tuning and task-specific calibration to ensure reliable deployment across different scenarios.

On the other hand, learning-based approaches have emerged as a promising alternative for controlling complex robotic systems. In particular, reinforcement learning (RL) demonstrating strong potential across a wide range of robotic control tasks, including dexterous manipulation [26], legged locomotion [36], and quadrotor flight [11]. Unlike model-based controllers that rely on explicit dynamics and structured formulations, reinforcement learning directly optimizes closed-loop behavior from interaction data. This allows RL policies to implicitly capture complex and unmodeled dynamics, while maintaining high-frequency inference suitable for real-time control. Leveraging large-scale parallel simulation, such policies have demonstrated strong robustness and generalization under complex and uncertain dynamics.

Despite these advances, applying RL to tilt-rotor aerial robots remains relatively unexplored. A primary challenge lies in the lack of a well-established learning formulation for this class of systems. The omnidirectional feature together with strong coupling between joint and rotor dynamics, makes it nontrivial to design training schemes that effectively guide black-box optimization toward stable and efficient 6D flight behaviors. A second challenge arises from sim-to-real transfer. While extensive domain randomization is often used to improve robustness, it can compromise control accuracy in favor of task-level success. For aerial robots, however, flight stability and precision are fundamental. Achieving reliable sim-to-real transfer therefore requires a careful balance between robustness and accuracy, particularly in the presence of significant modeling discrepancies and external disturbances.

In this paper, we demonstrate omnidirectional aerial motion on an overactuated tiltable quadrotor across diverse scenarios through RL controller, as shown in Fig. 1. The main contributions are summarized as follows:

- A reinforcement learning framework for overactuated tiltable quadrotors is proposed, enabling pose-reaching control with a single learned policy.
- Zero-shot deployment on real hardware is demonstrated by integrating system identification with domain randomization, balancing control accuracy and robustness.
- Extensive experiments and comparisons with NMPC are conducted, validating improved robustness and agility across diverse conditions.

II. RELATED WORK

A. Reinforcement Learning for Robot Control

RL has recently achieved remarkable success in robot control, particularly for systems with complex, high-dimensional, and strongly coupled dynamics [8]. In legged robotics, RL-based approaches have demonstrated agile and robust behaviors that are difficult to achieve with traditional model-based controllers, including rapid running [21], climbing and jumping [9], locomotion over unstructured terrain [12, 38], and recovery from diverse initial postures [10].

While model-based methods such as Model Predictive Control (MPC) provide strong theoretical guarantees, they often rely on accurate system models and require careful problem formulation and tuning to handle uncertainties [40, 6]. In contrast, RL learns control policies directly from data, enabling adaptation to unstructured environments and complex dynamics. Recent work has further shown that RL can implicitly capture feedback and planning-like behaviors, leading to fast transient responses and robust performance in challenging scenarios [21, 9].

Beyond legged robots, RL has also been successfully applied to aerial platforms, particularly quadrotors, demonstrating advantages in computational efficiency, robustness, and aggressive flight [11, 13, 42, 14, 32]. These studies highlight RL's potential as a general control paradigm for robotic systems with complex actuation and dynamics, and serve as important inspiration for extending learning-based control to tiltable aerial robots.

B. Motion Control for Tiltable Aerial Robot

Tiltable aerial robots enable 6D motion in $SE(3)$ by reorienting rotor thrust directions through rotation joints, but this capability comes at the cost of strongly coupled joint-rotor dynamics. Traditional model-based control methods occupy the mainstream position, mainly rely on classic control theory and optimal control [1, 30, 19, 18]. Early work employs linear-quadratic regulation with integral action and feedback linearization to achieve 6D pose tracking [1]. Subsequent approaches formulate quadratic programming or NMPC problems to explicitly handle joint angles, rotor thrusts, and actuation constraints [33, 19]. These methods can achieve accurate pose regulation and systematically enforce physical constraints, but typically require detailed system modeling and careful parameter tuning.

Based on the model-based framework, improving robustness is extended. Learned residual dynamics have been incorporated into MPC to compensate for modeling errors [3], while fault-tolerant control strategies reallocate thrust to maintain stability under actuator failures [34]. More recently, geometric and robust control methods have been applied to tiltable aerial robots equipped with manipulators, enabling full $SE(3)$ motion and interaction force compensation [18].

Despite these advances, the fundamental challenge of tiltable aerial robot control stems from the strong coupling between joint and rotor dynamics. This characteristic differentiates tiltable platforms from conventional quadrotors,

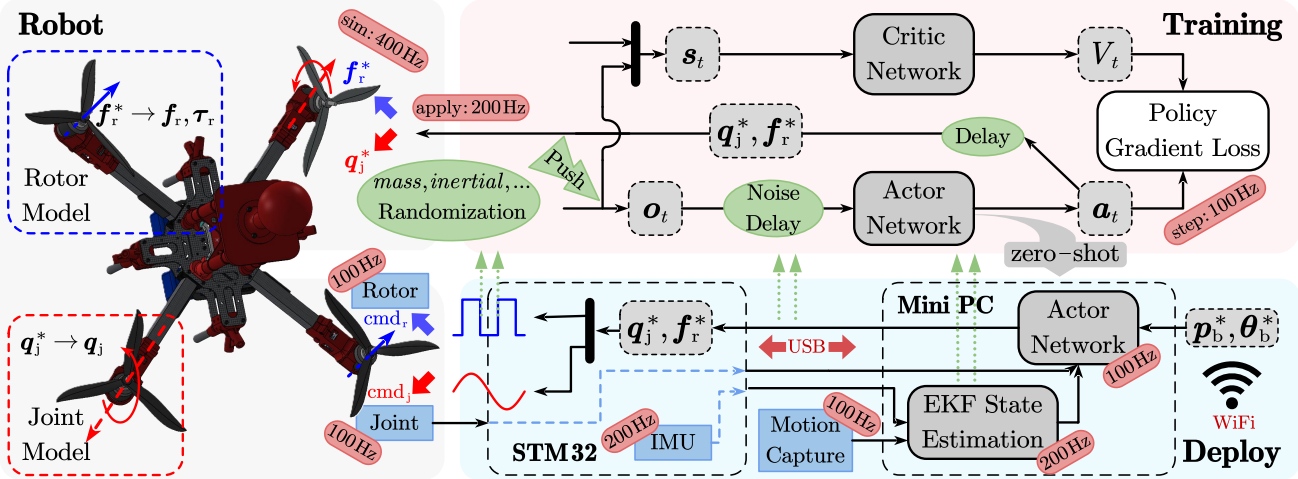


Fig. 2: Overall RL framework for system identification, training and deployment. **Robot:** Joint modules (red, target thrust $f_r^* \rightarrow$ real thrust f_r and torque τ_r), rotor modules (blue, joint position commands $q_j^* \rightarrow$ position feedback q_j), and system latency (green) are modeled to construct physically consistent simulation environments. **Training:** Policy is trained under asymmetric actor-critic framework and dynamics randomization (green) is integrated according to models and deployment scheme. **Deployment:** Trained policy is deployed on real robot platform with consistent system architecture. The robot’s state is estimated by fusing data from a motion capture system (MoCap) and an onboard IMU using an extended Kalman filter (EKF).

where actuation is dominated by rotor dynamics, and from legged robots, where actuation is primarily joint-based. Such coupled actuation introduces additional challenges in control formulation and sim-to-real transfer. Addressing these challenges in a unified and robust manner—while maintaining agile motion and fast transient response—remains an open problem. Motivated by this gap, we investigate learning-based control for overactuated tiltable quadrotors to enable robust and flexible omnidirectional aerial motion.

III. METHOD

We propose an RL framework for pose-reaching control, designed in accordance with the real robot platform and deployment scheme, as shown in Fig. 2.

A. Preliminaries

1) *Platform Introduction:* The tiltable quadrotor platform consists of four rotor modules mounted at the end of each arm. Each rotor module is equipped with a three-bladed 9-inch propeller driven by a T-Motor AT2814 KV900 brushless DC motor. A single-degree-of-freedom rotational joint is attached to each rotor module and actuated by a DYNAMIXEL XC330 T181-T servomotor. Details of physical parameters are shown in Appendix. V-A The rotor and joint modules constitute the core actuation components of the tiltable aerial robot, allowing thrust directions to be actively adjusted during flight. These components are also the primary focus of the system identification process described in Sec. III-C.

2) *Task Definition:* The control task is defined as reaching a target pose in the $SE(3)$ space and can be extended to continuously reaching a sequence of target poses. In contrast to velocity tracking or predefined trajectory tracking tasks commonly adopted in quadrotor and legged robot learning studies [15, 27], the proposed task emphasizes direct pose-level regulation.

3) *Problem Formulation:* The proposed RL problem is formulated as an infinite-horizon Partially Observable Markov Decision Process (POMDP), defined by the tuple $(\mathcal{S}, \mathcal{O}, \mathcal{A}, \mathcal{T}, d_0, r, \gamma)$, where $s \in \mathcal{S}$ denotes the full system state, $o \in \mathcal{O}$ represents a partial observation, and $a \in \mathcal{A}$ is the action space. The initial state distribution is given by d_0 , and the state transition dynamics are described by $\mathcal{T}(s_{t+1}|s_t, a_t)$. The reward function is denoted by $r(s_t, a_t)$ with a discount factor $\gamma \in [0, 1)$ [17]. The objective is to learn a policy $\pi_{\theta}(a|o)$, parameterized by θ , that maximizes the expected cumulative discounted reward $\mathbb{E}[\sum_{t=0}^{\infty} \gamma^t r(s_t, a_t)]$ over an infinite horizon.

B. Training Scheme

1) *Observation and Action Space:* The policy action a_t at time-step t is defined as

$$a_t = [a_{j,t}, a_{r,t}] \in \mathbb{R}^8 \quad (1)$$

where $a_{j,t} \in \mathbb{R}^4$ denotes the joint action and $a_{r,t} \in \mathbb{R}^4$ represents the rotor thrusts action. The joint actions are mapped to target joint position commands $q_{j,t}^* \in \mathbb{R}^4$ via

$$q_{j,t}^* = c_j a_{j,t}, \quad (2)$$

where c_j is a scale coefficient.

For aerial robot control, a nonzero baseline thrust is required to counteract gravity while maintain hovering. Accordingly, the target rotor thrusts $f_{r,t}^* \in \mathbb{R}^4$ applied to the robot are computed as

$$f_{r,t}^* = c_r a_{r,t} + C_f, \quad (3)$$

where c_r is a scale coefficient and C_f denotes the nominal hovering thrusts that approximately balances the gravitational force. This formulation allows the policy to output both positive and negative thrust adjustments around the hover operating point, facilitating efficient exploration during early training and promoting smoother thrust commands.

The dynamic actuator models for both the joint and rotor modules are obtained through system identification, expressing the relationship between control commands and actual response, as detailed in Sec. III-C2 and Sec. III-C3, respectively.

The policy observation $\mathbf{o}_t \in \mathbb{R}^{33}$ at time-step t is:

$$\mathbf{o}_t = [\mathbf{v}_{b,t}, \boldsymbol{\omega}_{b,t}, \mathbf{p}_{b,t}^*, R_{b,t}, R_{b,t}^*, \mathbf{q}_{j,t}, \mathbf{a}_{t-1}], \quad (4)$$

where the subscript b denotes robot base frame. $\mathbf{v}_{b,t} \in \mathbb{R}^3$ and $\boldsymbol{\omega}_{b,t} \in \mathbb{R}^3$ denote the base linear and angular velocity in base frame, respectively. $\mathbf{p}_{b,t}^* \in \mathbb{R}^3$ represents the desired position in base frame, while to facilitate reading $\mathbf{p}_w^* \in \mathbb{R}^3$ is defined as desired position in world frame. The current base orientation $R_{b,t} \in \mathbb{R}^6$ and desired orientation $R_{b,t}^* \in \mathbb{R}^6$ are encoded using a 6D normal-tangent representation [46], converted from quaternion or Euler-angle to ensure continuity and improve learning stability. $\mathbf{q}_{j,t} \in \mathbb{R}^4$ contains feedback joint positions, and \mathbf{a}_{t-1} denotes the action applied at the previous time-steps.

In real-world deployment, the agent has access only to partial observations, whereas additional state information is available in simulation during training. We therefore adopt an asymmetric actor-critic framework [25], in which the actor is conditioned solely on the observation \mathbf{o}_t available at deployment, while the critic is feed with a richer state \mathbf{s}_t during training. The critic state $\mathbf{s}_t \in \mathbb{R}^{41}$ is defined as

$$\mathbf{s}_t = [\mathbf{v}_{b,t}, \boldsymbol{\omega}_{b,t}, \mathbf{p}_{b,t}^*, R_{b,t}, R_{b,t}^*, \mathbf{q}_{j,t}, \boldsymbol{\tau}_{r,t}, \mathbf{f}_{r,t}, \mathbf{a}_{t-1}], \quad (5)$$

where the privileged variables include the rotor thrusts $\mathbf{f}_{r,t} \in \mathbb{R}^4$ and the corresponding thrust reaction torques $\boldsymbol{\tau}_{r,t} \in \mathbb{R}^4$.

2) *Reward Function*: The control objective is to drive the system toward a desired pose while maintaining smooth and stable motion. Rather than enforcing strict optimality, we define desirable performance as achieving fast convergence to the target pose with reduced oscillations and moderate control effort, consistent with commonly adopted criteria in model-based control methods. Accordingly, the reward function is composed of two main components: 1) pose reaching rewards, which encourages rapid convergence toward the desired pose; and 2) regularization rewards, which promote smooth, stable motion by discouraging excessive actuation and oscillatory behavior. The detailed reward terms and their corresponding weights are summarized in Table. I. Here, $\mathbf{p}_e = \mathbf{p}_b - \mathbf{p}_b^*$ denotes the desired position error and $\boldsymbol{\theta}_e = \boldsymbol{\theta}_b - \boldsymbol{\theta}_b^*$ represents the desired orientation error, where $\boldsymbol{\theta}_b$ and $\boldsymbol{\theta}_b^*$ are the current base orientation and desired base orientation in Euler angles, respectively. b_z and b_z^* denotes body frame z -axes of the current and desired base frame, expressed in the world frame.

Desired Position term encourages the robot to approach the target position, while *Desired Pose* term promotes alignment with the target orientation as the robot converge to target position. *Reach Position* and *Reach Pose* rewards provide sparse bonuses when the robot reaches the target position or full pose within the specified thresholds and maintains a stable state. The regularization terms include *Linear Velocity* and *Angular Velocity* penalties, which discourage excessive body motion and promote stable flight behavior. Unlike pose-reaching formulations commonly adopted in legged robot

TABLE I: Reward Description

Reward	Formulation	Weight
Pose Reaching		
Desired Position	$\tanh\left(\frac{\ \mathbf{p}_e\ }{0.6}\right)$	-1.0
Desired Pose	$\left(1 - \tanh\left(\frac{\ \boldsymbol{\theta}_e\ }{2}\right)\right) \times \left(1 - \tanh\left(\frac{\ \mathbf{p}_e\ }{2}\right)\right)$	2.0
Reach Position	$[(\ \mathbf{p}_e\ < 0.02) \& (\ \mathbf{v}_b\ < 0.02)] \times \left[e^{-\frac{\ \mathbf{p}_e\ }{0.02}} + e^{-\frac{\ \mathbf{v}_b\ }{0.02}}\right]$	1.0
Reach Pose	$\left[(\ \mathbf{p}_e\ < 0.02) \& (\ \boldsymbol{\theta}_e\ < 0.05)\right] \& (\ \mathbf{v}_b\ < 0.02) \& (\ \boldsymbol{\omega}_b\ < 0.02)] \times \left[e^{-\frac{\ \mathbf{p}_e\ }{0.02}} + e^{-\frac{\ \boldsymbol{\omega}_b\ }{0.02}} + e^{-2\frac{\ \boldsymbol{\theta}_e\ }{0.05}} + e^{-2\frac{\ \boldsymbol{\omega}_b\ }{0.02}}\right]$	0.75
Regularization		
Linear Velocity	$(e^{0.6 \cdot \min(\ \mathbf{v}_b\ , 4.0)} - 1)^2$	-0.03
Angular Velocity	$(e^{0.4 \cdot \min(\ \boldsymbol{\omega}_b\ , 6.0)} - 1)^2$	-0.05
Joint Limitation	$\sum_i^4 (q_i^* - \bar{q} (q_i^* > \bar{q}))^2$	-0.02
Thrust Limitation	$\sum_i^4 (f_{i,t}^* - \bar{f})^2$	-0.01
Joint Action Rate	$\sum_i^4 (q_{i,t}^* - q_{i,t-1}^*)^2$	-5.0×10^{-4}
Thrust Action Rate	$\sum_i^4 (f_{i,t}^* - f_{i,t-1}^*)^2$	-1.0×10^{-4}
Thrust Power	$\sum_i^4 f_i^2$	-1.0×10^{-5}
Joint Acceleration	$\sum_i^4 (\ddot{q}_{i,t} - \ddot{q}_{i,t-1})^2$	-1.5×10^{-5}
<i>z-Axis Align</i>	$ b_z - b_z^* > 1.5$	-0.1
Thrust Allocation	$\sum_i^4 \left(f_{i,t}^* - \frac{\sum_j^4 f_{j,t}^*}{4}\right)^2 b_z^2$	-1.0×10^{-5}

learning [27, 2], we avoid explicit time- or reference-velocity-based rewards that enforce reaching the target pose within a prescribed duration. Instead, the reward design balances task completion, energy efficiency, and motion smoothness, allowing the policy to autonomously discover control strategies that achieve agile yet stable pose convergence. Additional regularization terms penalize actuator limit violations, abrupt action changes, excessive thrust power, and large joint accelerations, promoting smooth and efficient control. Finally, the *z-Axis Align* and *Thrust Allocation* terms are heuristically designed to encourage an even distribution of rotor thrust across varying base orientations, resulting in balanced actuator workloads.

3) *Initial State Distribution*: Target poses are uniformly sampled in the $SE(3)$ space. The desired position $\mathbf{p}_w^* \in \mathbb{R}^3$ is sampled within a $4\text{ m} \times 4\text{ m} \times 3\text{ m}$ region and converted to the base frame, while the desired orientation $\boldsymbol{\theta}_b^* \in \mathbb{R}^3$ is drawn from a uniform axis-angle distribution in $[-\pi, \pi]$. The robot is initialized at the origin with zero linear and angular velocities, and its initial orientation is also uniformly sampled in axis-angle form. The initial joint position $\mathbf{q}_{j,0}$ is critical, as static hovering is feasible only at specific joint configurations within $[-\pi, \pi]$ work range. To encourage exploration while maintaining training stability, $\mathbf{q}_{j,0}$ is initialized in a stratified manner across parallel environments, as $\mathbf{q}_{j,0} = -\pi$ or $\mathbf{q}_{j,0} = 0$ or $\mathbf{q}_{j,0} = \pi$ or $\mathbf{q}_{j,0} \in \{-\pi, 0, \pi\}$ with equal proportions.

C. Sim-to-Real Transfer

1) *System Latency*: Communication latency is unavoidable in real-world robotic systems and can degrade control performance or even cause instability if unmodeled. To address this issue, we explicitly incorporate time delays into the training process by executing delayed joint position and rotor commands and providing delayed joint position observation to ensure consistency between training and deployment. Such latency also incorporates dynamic response delays from the actuator modules, which is highlighted in previous studies [4].

In addition to actuation latency, observation delays are also present due to state estimation. The onboard Kalman-filter-based estimator fuses motion capture and IMU measurements, introducing an additional delay in velocity estimates. This delay is likewise modeled during training by providing the policy with delayed velocity observations.

2) *Rotor Model*: The rotor module serves as the primary actuator of the aerial robot, as it is responsible for generating the forces and torques required for motion. In real-world operation, rotor thrust dynamics are highly nonlinear and influenced by motor characteristics, propeller aerodynamics, and power supply voltage, making accurate analytical modeling difficult. We therefore empirically identify the rotor thrust and torque characteristics by collecting real-world data under a range of PWM commands and supply voltages using a 6-axis force-torque sensor, details are illustrated in Appendix. V-B. Polynomial functions are fitted to map the PWM command cmd_r and voltage V_r to the generated thrust and torque, as:

$$\begin{cases} \mathbf{f}_r = \mathbf{f}_r(\text{cmd}_r, V_r) \\ \boldsymbol{\tau}_r = C_\Omega \mathbf{f}_r \end{cases}, \quad (6)$$

where C_Ω denotes the torque-to-thrust ratio. In simulation, the identified thrust and torque are directly applied as external forces and torques on the rotor links:

$$\mathbf{f}_{r,t} = \mathbf{f}_{r,t}^*, \quad \boldsymbol{\tau}_{r,t} = C_\Omega \mathbf{f}_{r,t} \quad (7)$$

During real-world deployment, the corresponding PWM command is obtained via the inverse mapping::

$$\text{cmd}_{r,t} = \mathbf{f}_r^{-1}(\mathbf{f}_{r,t}^*, V_r) \quad (8)$$

3) *Joint Model*: Accurate joint motor modeling is critical for articulated aerial robots, as the direction of rotor-generated thrust and torque is directly determined by the joint angles, fundamentally distinguishing them from fixed-rotor platforms. In generally used simulators for multi-rigid-body dynamics, rotational joints are commonly modeled as DC motors with proportional-derivative (PD) position control:

$$\tau = K_p(q_j^* - q_j) - K_d\dot{q}_j, \quad (9)$$

where q_j and \dot{q}_j denotes the joint position and velocity, and K_p and K_d correspond to stiffness and damping coefficients. For such actuators, the joint dynamics can be approximated by a second-order system

$$\tau = J\ddot{q}_j, \quad (10)$$

leading to the transfer function

$$\frac{q_j(s)}{q_j^*(s)} = \frac{K_p}{Js^2 + K_d s + K_p}, \quad (11)$$

with natural frequency ω_n and damping ratio ζ given by

$$\omega_n^2 = \frac{K_p}{J}, \quad 2\zeta\omega_n = \frac{K_d}{J}. \quad (12)$$

where J represents the effective rotational inertia. The parameters ω_n and ζ can be identified from real joint response data and then used to compute the corresponding stiffness K_p and damping coefficients K_d for simulated joints, details are shown in Appendix. V-C. In addition, joint torque and velocity limits can also be measured experimentally. During real-world deployment, the joint position commands $\text{cmd}_{q,t}$ are directly set as $q_{j,t}^*$

4) *Domain Randomization and Noise*: To mitigate the physical difference between simulation and reality, we employ domain randomization, noise and random disturbance during training. Domain randomization has been widely adopted to enhance the robustness of learned policies and facilitate sim-to-real transfer but is a trade off the optimality [36]. Therefore, we just adopt minimal domain randomization in our training environments, including body mass, body inertia, and joint position offsets. Other commonly used parameters, such as rotor thrust coefficients, joint stiffness and damping coefficients, and aerodynamic drag, are intentionally not randomized [4, 38]. In addition, observation noise is injected to account for sensor uncertainties encountered in practice. This restrained randomization strategy improves policy generalization to the physical robot while preserving fast response and stable behavior. The complete set of randomization, noise parameters and latency used during training are summarized in Appendix. V-D.

IV. EXPERIMENTS

A. Experimental Setup

We construct the training environment using Isaac Sim [24] and Isaac Lab [22], and optimize the policy using proximal policy optimization (PPO) [28] as implemented in the RSL-RL framework [29]. Training is performed on an NVIDIA A10 GPU, and the detailed training hyperparameters are provided in the Appendix. V-E. The learned policy is directly deployed in both simulation and real-world experiments without any fine-tuning. Results obtained using the reinforcement learning approach are labeled as RL and shown in blue in all figures of this section.

As a baseline, the NMPC controller is implemented following [19], with nonlinear optimization solved using acados [37]. The NMPC controller runs at 100 Hz on the onboard computer and is fully integrated into the robot system architecture, serving as the control module analogous to the actor network in the reinforcement learning framework, as illustrated in Fig. 2. All NMPC parameters remain fixed throughout the experiments to ensure a fair comparison. Results obtained using NMPC are labeled as NMPC and shown in red in all figures of this section.

TABLE II: Continuous Pose Reaching in Simulation

	$\mathcal{U} \ p_e \ (min, max)[m]$	$\mathcal{U} \ \theta_e \ (min, max)[deg]$	$\mathcal{L} \ p_e \ (min, max)[m]$	$\mathcal{L} \ \theta_e \ (min, max)[deg]$	$\ v_b \ (\pm std)[m/s]$	$\ \omega_b \ (\pm std)[rad/s]$	$ q_i^* - q (\pm std)[rad]$	$f_r^* (\pm std)[N]$
NMPC	0.02 (0.002, 0.116)	40.99 (0.41, 136.97)	0.31 (0.09, 0.76)	51.75 (6.38, 143.15)	0.008 (± 0.0005)	0.007 (± 0.003)	0.004 (± 0.011)	9.17 (± 3.48)
RL	0.08 (0.014, 0.232)	5.89 (0.34, 85.49)	0.18 (0.06, 0.58)	13.59 (0.75, 104.35)	0.015 (± 0.049)	0.012 (± 0.044)	0.026 (± 0.074)	10.08 (± 3.36)

B. Simulation Experiments

We construct standalone simulation environments based on Gazebo and use the same control framework to make fair comparison between learned policy and NMPC controller.

1) *Waypoints Hovering*: We first evaluated waypoint hovering performance by sampling 100 random target poses in the $SE(3)$ space following the same sampling scheme used during training. The robot was commanded to reach each target pose sequentially within an 8 s horizon to assess overall continuous pose-reaching capability. Results are summarized in Table. II, where $\mathcal{U}(\cdot)$ denotes the average value during hovering at the target pose (7.0-7.5s of the 8 s horizon), indicating accuracy, and $\mathcal{L}(\cdot)$ represents the average value over the flight phase (1.0-7.0s of the 8 s horizon), indicating agility.

The results indicate that both controllers can successfully reach random target poses in the $SE(3)$ space. NMPC achieves lower position error, while RL demonstrates better orientation accuracy. In Fig. 3, the orientation errors under NMPC exhibit a more dispersed distribution, which may be attributed to sensitivity of the nonlinear optimization to local minima under certain operating conditions. Moreover, RL attains fast convergence to the target pose, as the accumulated position and orientation errors over the entire trajectory are lower than those of NMPC. Body velocity statistics further confirm stable flight under both controllers. While RL shows marginally higher joint position errors and average thrust commands, this behavior is consistent with its more agile maneuvers during pose reaching.

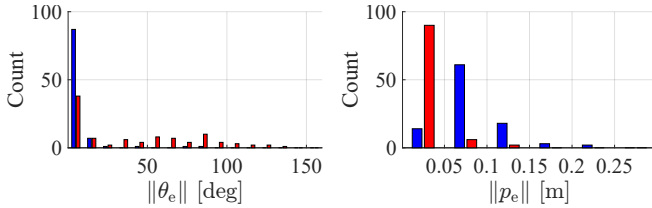


Fig. 3: Statistical distributions of position and orientation errors during stable hovering at the sampled target poses.

2) *Disturbance Rejection*: To evaluate disturbance rejection performance, external forces and torques are applied to the robot while it maintains stable hovering at $p_w^* = [0 \ 0 \ 1.5] \text{ m}$, $\theta_b^* = [25 \ 0 \ 0] \text{ deg}$. Two types of disturbances are considered: 1) a continuous external force applied along the z -axis for 2 seconds, and 2) an impulsive torque applied about the x -axis for 0.05 seconds. Quantitative statistics of the pose errors under these disturbances are illustrated in Fig. 4. Both controllers are able to reject moderate disturbances and maintain stable flight. Under continuous force disturbances, the RL policy exhibits stronger disturbance rejection capability, resulting in smaller position and orientation deviations

compared to NMPC. When the applied external force reaches 100 N, both controllers lose stability. For impulsive torque disturbances, different performance regimes are observed. When the applied impulse torque is below 15 Nm, the RL policy exhibits faster recovery to the target pose, indicating superior transient disturbance rejection performance. In the intermediate range between 15 Nm and 25 Nm, NMPC shows more stable performance with continuous enlarged pose errors, but RL loses stability rapidly. When the impulse torque exceeds 25 Nm, neither controller is able to restore stability, but RL shows slightly smaller peak pose errors.

These results indicate that the learned policy provides improved transient disturbance rejection under moderate impulsive disturbances, while the ultimate disturbance rejection limits of both controllers are constrained by the physical actuation capabilities of the platform, such as maximum achievable rotor thrust.

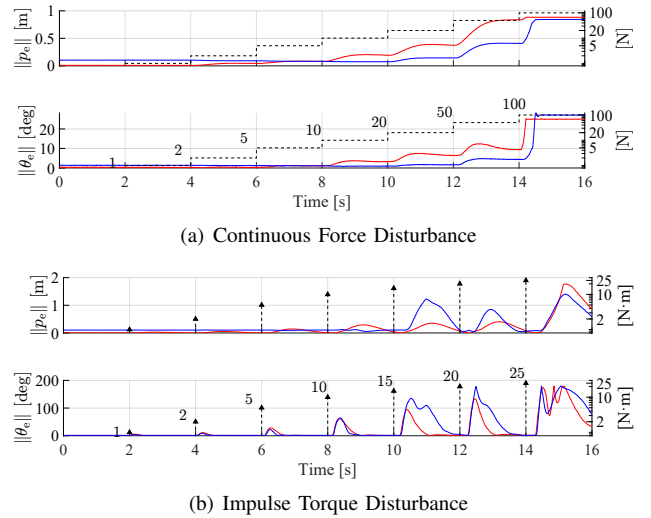


Fig. 4: Disturbance rejection evaluation results under time-varying external forces and torques. The disturbances are updated every 2 s, and the black dashed lines denote their magnitudes.

C. Real-world Experiments

Zero-shot performance is evaluated through real-world experiments and against an NMPC controller. The robot is equipped with an onboard computer KHADAS VIM4, containing a 2.2GHz Quad-Core ARM Cortex-A73 and a 2.0GHz Quad-Core Cortex-A53 CPU for high-level computation and a STM32 embedded system for low-level control. The VIM4 runs Ubuntu 20.04 and ROS Noetic for state estimation and policy inference and also for optimization solving of NMPC. Notably, forward inference of the RL policy consistently requires approximately 0.3 ms on average, whereas NMPC optimization typically completes within a 10 ms control period but occasionally exceeds this time budget.

1) *Waypoints Hovering*: The robot is commanded to sequentially reach a set of predefined target poses with a period of 8 seconds, and the pose-reaching task is repeated three times. Quantitative performance metrics are summarized in Table. III, while the snapshots are shown in Fig. 1(a) and the corresponding state trajectories are shown in Fig. 5.

TABLE III: Continuous Pose Reaching in Real-world

p_b^* [m]	θ_b^* [deg]	RL		NMPC	
		$\mathcal{L} \ p_e \ $ [m]	$\mathcal{L} \ \theta_e \ $ [deg]	$\mathcal{L} \ p_e \ $ [m]	$\mathcal{L} \ \theta_e \ $ [deg]
[0.0, 0.0, 0.8]	[0.0, 0.0, 0.0]	0.114	2.589	0.026	2.644
[1.0, 0.0, 1.0]	[45.0, 0.0, 0.0]	0.060	4.350	0.074	4.372
[0.0, 1.0, 1.0]	[0.0, -25.0, 0.0]	0.046	4.214	0.054	8.225
[-1.0, 0.0, 1.0]	[-25.0, 0.0, 0.0]	0.074	5.561	0.028	4.742
[0.0, 0.0, 0.8]	[0.0, 0.0, 90.0]	0.091	4.590	0.028	1.768
Mean		0.077	4.261	0.042	4.350

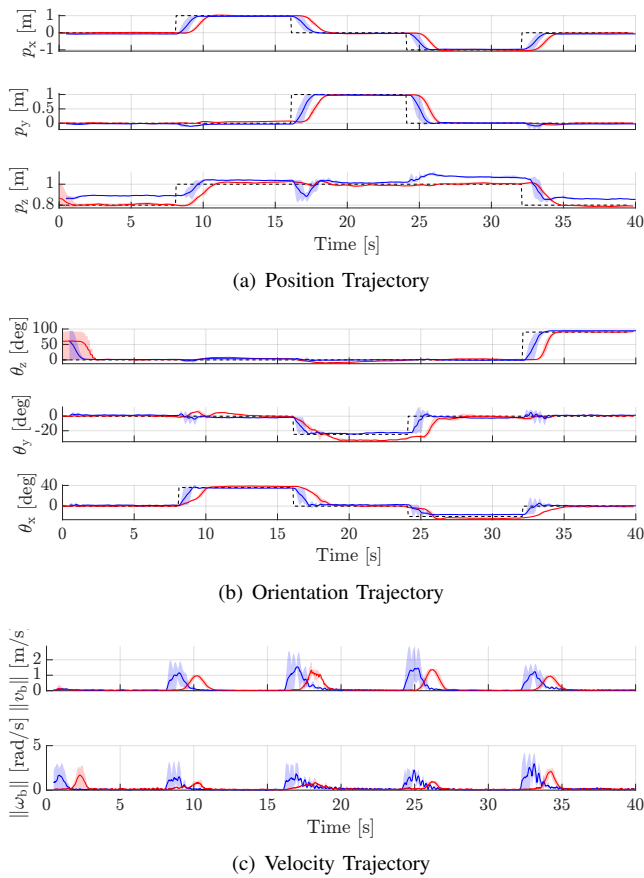


Fig. 5: State trajectories from real-world continuous pose-reaching experiments. Solid lines show the mean values across trials, and the shaded regions represent the corresponding minimum and maximum ranges.

The results indicate that the RL policy achieves position accuracy comparable to NMPC while attaining improved orientation accuracy in real-world experiments, consistent with the simulation results. In addition, NMPC exhibits pose-dependent orientation errors across different target poses, whereas the RL policy maintains more consistent orientation accuracy throughout the sequence. The state trajectories shown in Fig. 5 further demonstrate that the RL policy produces more

agile motions than NMPC. Specifically, pose errors converge more rapidly under RL control, and the corresponding velocity profiles support this observation: the RL policy reaches higher peak linear and angular velocities during pose transitions (exceeding 2 m/s and approaching 5 rad/s, respectively), while remaining stable. This improved transient behavior aligns with observations in [16], which report that reinforcement learning controllers typically achieve superior transient performance.

2) *Disturbance Rejection*: We evaluate disturbance rejection performance in real-world experiments, shown in Fig. 1(c) and Fig. 1(d). The robot maintains stable hovering at $p_w^* = [0 \ 0 \ 1.0]$ m, $\theta_b^* = [0 \ 0 \ 0]$ deg, while external disturbances are applied in two forms: 1) continuous wind disturbance generated by a fan, and 2) impulsive stick pushes applied to the robot body. The resulting pose errors and velocity trajectories are shown in Fig. 6. Both controllers are able to maintain stable flight under moderate disturbances. Under wind disturbance, the RL policy exhibits smaller position and orientation fluctuations, with reduced standard deviations in position error (0.005 vs. 0.028 m) and orientation error (0.63 vs. 1.32 deg) compared to NMPC. However, RL shows a larger mean steady-state position offset (0.10 vs. 0.04 m) while maintaining a smaller mean orientation error (3.55 vs. 4.27 deg), consistent with the pose-reaching results discussed earlier. For impulsive stick disturbances, the RL policy recovers to the target pose more rapidly than NMPC. This behavior is reflected in sharper but shorter velocity peaks, accompanied by lower average linear and angular velocities (0.025 vs. 0.033 m/s and 0.081 vs. 0.092 rad/s, respectively), indicating improved transient disturbance rejection performance. These results further validate the effectiveness of the proposed learning-based control approach in handling real-world disturbances.

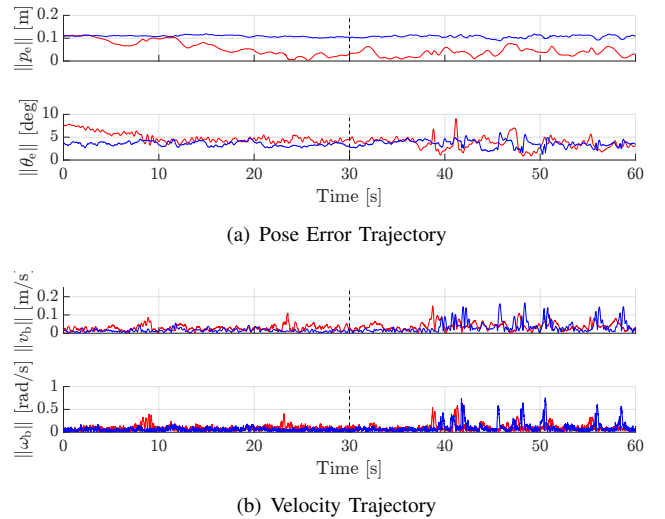


Fig. 6: Real-world disturbance rejection evaluation. The former part shows the response under wind disturbances, while the later part presents the response to impulsive stick pushes.

We further evaluate payload adaptation by attaching additional weights to the robot during hovering tasks, also shown in Fig. 1(e). The resulting position and orientation

errors are shown in Fig. 7. As expected, increasing payload mass primarily affects the vertical (z -axis) position for both RL and NMPC due to changes in the effective gravitational load, which is consistent with the continuous external force disturbance experiments in simulation. In contrast, orientation errors remain relatively stable across the tested payload conditions and do not exhibit significant variations. These observations indicate that, within the evaluated payload range, both controllers maintain robust orientational regulation, while vertical position deviations are mainly constrained by available thrust authority.

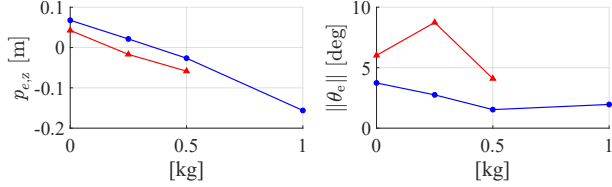


Fig. 7: Real-world hovering experiments under different payload weights. 1.0 kg weight evaluation is not conducted for NMPC due to safety concerns.

D. Extended Studies

Although the policy is trained only for target pose reaching, we further evaluate its generalization to trajectory tracking tasks in real-world, as shown in Fig. 1(b). The reference trajectory is defined as a time-parameterized 3D lemniscate with synchronized orientational modulation (Roll and Pitch within 0.5 rad and Yaw in $[0, 2\pi]$). The tracking task is repeated 5 times, and the results are illustrated in Fig. 8. It is

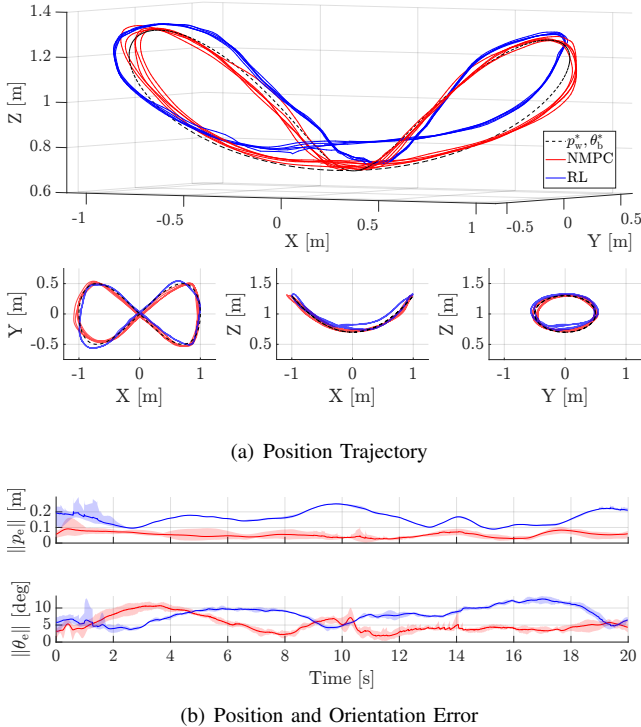


Fig. 8: Real-world trajectory tracking results. Solid lines show the mean values across trials, and the shaded regions represent the corresponding minimum and maximum ranges.

noteworthy that, despite being trained solely for pose-reaching tasks, the learned policy demonstrates effective trajectory tracking capability and generalization. While the RL exhibits larger average position and orientation errors compared to NMPC (0.16 m vs. 0.05 m and 8.06 deg vs. 5.19 deg, respectively), it achieves comparable variability in tracking performance, with similar standard deviations in position error (0.04 vs. 0.02) and orientation error (2.45 vs. 2.46). These results indicate that the RL policy is able to maintain stable tracking behavior along a continuous, time-varying trajectory, despite not being explicitly trained for trajectory tracking. This highlights the strong generalization capability of the learned policy to dynamic control tasks beyond its original training scope. These results suggest that the RL controller behaves as a low-level feedback motion controller, leading to robust and stable tracking behavior in dynamic tasks.

E. Limitation Discussion

Despite the demonstrated agile and robust motion capabilities, several limitations of the proposed approach are identified through experimental evaluation.

First, the performance of the learned policy depends on sufficiently system identification before training to preserve physical consistency. Significant sim-to-real discrepancies may degrade performance, particularly during aggressive pose transitions (e.g., $90/180$ deg of roll/pitch angles). Changes in actuator characteristics, such as joint or rotor dynamics, would therefore require re-identification and retraining. Future work may explore online adaptation to improve robustness under modeling uncertainties and time-varying dynamics.

Second, the current platform operates within a bounded joint workspace of $[-1.25\pi, 1.25\pi]$, and certain pose transitions may approach joint singularities, potentially compromising motion stability. While model-based controllers can explicitly handle such singularities through optimization, the proposed RL approach does not explicitly reason about singularity avoidance. Future research may integrate model-based strategies and improved training curricula to better address joint singularities and expand the achievable motion envelope.

V. CONCLUSION

This paper presents a learning-based approach for agile and robust six-degree-of-freedom pose control of an overactuated tilttable quadrotor. By leveraging reinforcement learning with carefully designed training strategies, the proposed controller effectively handles the strongly coupled joint-rotor dynamics. Extensive experimental results demonstrate flexible pose reaching, stable trajectory tracking, and effective disturbance rejection in both simulation and real-world settings.

Compared with state-of-the-art model-based controllers, the proposed approach achieves improved robustness and faster transient response while maintaining low computational overhead suitable for onboard deployment. Future work will focus on further enhancing robustness and accuracy, and extending the framework toward whole-body control of more complex tilttable aerial robots.

APPENDIX

A. Physical Parameters

The physical parameters of the robot are summarized in Table IV.

TABLE IV: Physical Parameters

Term	Value
mass [kg]	3.0386
motor-to-motor diagonal distance [m]	0.55
diagonal inertia I_{xx}, I_{yy}, I_{zz} [kg·m ²]	0.0627, 0.0620, 0.0948
joint position limit \bar{q} [rad]	3.96
thrust limit \bar{f} [N]	20

B. Rotor Module System Identification

The rotor module identification process involved measuring the thrust and torque outputs of the rotors at different PWM commands and power supply voltages. Fig. 9 illustrates the relationship between rotor thrust and torque under varying power supply voltage and PWM commands. The identified torque-to-thrust ratio $C_{\Omega} = 0.0165$.

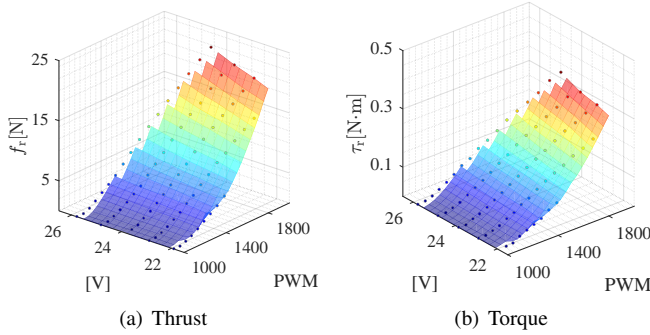


Fig. 9: Relationship between rotor thrust and torque under varying power supply voltage and PWM commands.

C. Joint Module System Identification

The system identification process involved collecting real-world joint position responses at 200 Hz under sinusoidal excitation with gradually varying amplitude. Fig. 10 shows the measured joint responses and the corresponding simulated results obtained using the identified model. The identified joint model parameters are summarized in Table V.

TABLE V: Joint Model Parameters

Term	Value
K_p	0.3449
K_d	0.0094
velocity limit [rad/s]	10.0
effort limit [N·m]	3.0

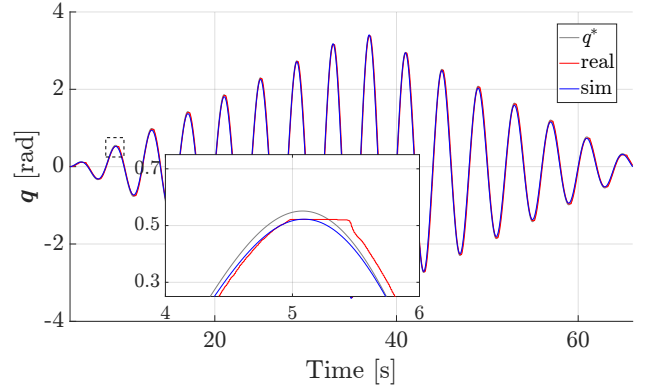


Fig. 10: Joint Model Identification Response. q^* is the desired joint position, *sim* is identified model response in simulation environments, and *real* is the actual joint position response.

D. Dynamic Randomization

The dynamic randomization parameters are summarized in Table VI.

TABLE VI: Domain Randomization, Noise and Time Delay

Variables	Operation	Latency(dt)
Dynamics Parameters		
mass [kg]	scale [0.95,1.05]	-
inertia [kg·m ²]	scale [0.95,1.05]	-
COM [m]	bias ± 0.01	-
State Observations		
p_b [m]	bias ± 0.01 , noise ± 0.01	0
θ_b [deg]	bias ± 0.01 , noise ± 0.01	0
v_b [m/s]	bias ± 0.005 , noise ± 0.005	3~5
ω_b [rad/s]	bias ± 0.005 , noise ± 0.005	3~5
q_j [deg]	bias ± 3 , noise ± 2	1~2
Action Commands		
a_j [rad]	-	1~3
a_r [N]	-	1~3

E. Training Details

The training hyperparameters are summarized in Table VII.

TABLE VII: Hyperparameters

Hyperparameter	Value
General	
num of robots	4096
num of steps per iteration	48
num of epochs	5
gradient clipping	1.0
adam epsilon	$1e - 8$
PPO	
clip range	0.2
entropy coefficient	$5.0e - 4$
discount factor γ	0.99
GAE balancing factor λ	0.95
desired KL-divergence	0.01
actor and critic NN	MLP, hidden units [512, 256, 128]
Specific	
joint scale coefficient c_j	0.25
rotor scale coefficient c_r	0.5

REFERENCES

- [1] Mike Allenspach, Karen Bodie, Maximilian Brunner, Luca Rinzsoz, Zachary Taylor, Mina Kamel, Roland Siegwart, and Juan Nieto. Design and optimal control of a tiltrotor micro-aerial vehicle for efficient omnidirectional flight. *The International Journal of Robotics Research*, 39(10-11):1305–1325, 2020.
- [2] Qingwei Ben, Botian Xu, Kailin Li, Feiyu Jia, Wentao Zhang, Jingping Wang, Jingbo Wang, Dahua Lin, and Jiangmiao Pang. Gallant: Voxel grid-based humanoid locomotion and local-navigation across 3d constrained terrains. *arXiv preprint arXiv:2511.14625*, 2025.
- [3] Maximilian Brunner, Weixuan Zhang, Ahmad Roumie, Marco Tognon, and Roland Siegwart. Mpc with learned residual dynamics with application on omnidirectional mavs. *arXiv preprint arXiv:2207.01451*, 2022.
- [4] Jiayu Chen, Chao Yu, Yuqing Xie, Feng Gao, Yinuo Chen, Shu’ang Yu, Wenhao Tang, Shilong Ji, Mo Mu, Yi Wu, et al. What matters in learning a zero-shot sim-to-real rl policy for quadrotor control? a comprehensive study. *IEEE Robotics and Automation Letters*, 2025.
- [5] Dario Floreano and Robert J Wood. Science, technology and the future of small autonomous drones. *nature*, 521(7553):460–466, 2015.
- [6] Ruben Grandia, Fabian Jenelten, Shaohui Yang, Farbod Farshidian, and Marco Hutter. Perceptive locomotion through nonlinear model-predictive control. *IEEE Transactions on Robotics*, 39(5):3402–3421, 2023.
- [7] Harsh Gupta, Xiaofeng Guo, Huy Ha, Chuer Pan, Muqing Cao, Dongjae Lee, Sebastian Sherer, Shuran Song, and Guanya Shi. Umi-on-air: Embodiment-aware guidance for embodiment-agnostic visuomotor policies. *arXiv preprint arXiv:2510.02614*, 2025.
- [8] Sehoon Ha, Joonho Lee, Michiel van de Panne, Zhaoming Xie, Wenhao Yu, and Majid Khadiv. Learning-based legged locomotion: State of the art and future perspectives. *The International Journal of Robotics Research*, 44(8):1396–1427, 2025.
- [9] David Hoeller, Nikita Rudin, Dhionis Sako, and Marco Hutter. Anymal parkour: Learning agile navigation for quadrupedal robots. *Science Robotics*, 9(88):eadi7566, 2024.
- [10] Tao Huang, Junli Ren, Huayi Wang, Zirui Wang, Qingwei Ben, Muning Wen, Xiao Chen, Jianan Li, and Jiangmiao Pang. Learning humanoid standing-up control across diverse postures. In *Robotics: Science and Systems (RSS)*, 2025.
- [11] Jemin Hwangbo, Inkyu Sa, Roland Siegwart, and Marco Hutter. Control of a quadrotor with reinforcement learning. *IEEE Robotics and Automation Letters*, 2(4):2096–2103, 2017.
- [12] Jemin Hwangbo, Joonho Lee, Alexey Dosovitskiy, Dario Bellicoso, Vassilios Tsounis, Vladlen Koltun, and Marco Hutter. Learning agile and dynamic motor skills for legged robots. *Science Robotics*, 4(26):eaau5872, 2019.
- [13] Elia Kaufmann, Leonard Bauersfeld, and Davide Scaramuzza. A benchmark comparison of learned control policies for agile quadrotor flight. In *2022 International Conference on Robotics and Automation (ICRA)*, pages 10504–10510. IEEE, 2022.
- [14] Elia Kaufmann, Leonard Bauersfeld, Antonio Loquercio, Matthias Müller, Vladlen Koltun, and Davide Scaramuzza. Champion-level drone racing using deep reinforcement learning. *Nature*, 620(7976):982–987, 2023.
- [15] William Koch, Renato Mancuso, Richard West, and Azer Bestavros. Reinforcement learning for uav attitude control. *ACM Transactions on Cyber-Physical Systems*, 3(2):1–21, 2019.
- [16] Pratik Kunapuli, Jake Welde, Dinesh Jayaraman, and Vijay Kumar. Leveling the Playing Field: Carefully Comparing Classical and Learned Controllers for Quadrotor Trajectory Tracking. In *Proceedings of Robotics: Science and Systems*, Los Angeles, CA, USA, June 2025. doi: 10.15607/RSS.2025.XXI.116.
- [17] Mikko Lauri, David Hsu, and Joni Pajarinen. Partially observable markov decision processes in robotics: A survey. *IEEE Transactions on Robotics*, 39(1):21–40, 2022.
- [18] Dongjae Lee, Byeongjun Kim, and Hyoun Jin Kim. Autonomous aerial manipulation at arbitrary pose in se (3) with robust control and whole-body planning. *The International Journal of Robotics Research*, page 02783649251378195, 2025.
- [19] Jinjie Li, Junichiro Sugihara, and Moju Zhao. Servo integrated nonlinear model predictive control for overactuated tilttable-quadrotors. *IEEE Robotics and Automation Letters*, 9(10):8770–8777, 2024.
- [20] Zhan Li, Yipeng Yang, Xinghu Yu, Cuiyu Liu, Okyay Kaynak, and Huijun Gao. Fixed-time control of a novel thrust-vectoring aerial manipulator via high-order fully actuated system approach. *IEEE/ASME Transactions on Mechatronics*, 30(2):1084–1095, 2024.
- [21] Gabriel B Margolis, Ge Yang, Kartik Paigwar, Tao Chen, and Pulkit Agrawal. Rapid locomotion via reinforcement learning. *The International Journal of Robotics Research*, 43(4):572–587, 2024.
- [22] Mayank Mittal, Pascal Roth, James Tigue, Antoine Richard, Octi Zhang, Peter Du, Antonio Serrano-Muñoz, Xinjie Yao, René Zurbrugg, Nikita Rudin, Lukasz Wawrzyniak, Milad Rakhsha, Alain Denzler, Eric Heiden, Ales Borovicka, Ossama Ahmed, Iretyayo Akinola, Abrar Anwar, Mark T. Carlson, Ji Yuan Feng, Animesh Garg, Renato Gasoto, Lionel Gulich, Yijie Guo, M. Gussert, Alex Hansen, Mihir Kulkarni, Chenran Li, Wei Liu, Viktor Makoviyuchuk, Grzegorz Malczyk, Hammad Mazhar, Masoud Moghani, Adithyavairavan Murali, Michael Noseworthy, Alexander Poddubny, Nathan Ratliff, Welf Rehberg, Clemens Schwarke, Ritvik Singh, James Latham Smith, Bingjie Tang, Ruchik Thaker, Matthew Trepte, Karl Van Wyk, Fangzhou Yu, Alex Milane, Vikram Ramasamy, Remo Steiner, Sangeeta Sub-

- ramanian, Clemens Volk, CY Chen, Neel Jawale, Ashwin Varghese Kuruttukulam, Michael A. Lin, Ajay Mandlekar, Karsten Patzwaladt, John Welsh, Jean-Francois Lafleche, Nicolas Moëne-Loccoz, Soowan Park, Rob Stepinski, Dirk Van Gelder, Chris Amever, Jan Carius, Jumyung Chang, Anka He Chen, Pablo de Heras Ciechowski, Gilles Daviet, Mohammad Mohajerani, Julia von Muralt, Viktor Reutsky, Michael Sauter, Simon Schirm, Eric L. Shi, Pierre Terdiman, Kenny Vilella, Tobias Widmer, Gordon Yeoman, Tiffany Chen, Sergey Grizan, Cathy Li, Lotus Li, Connor Smith, Rafael Wiltz, Kostas Alexis, Yan Chang, Linxi "Jim" Fan, Farbod Farshidian, Ankur Handa, Spencer Huang, Marco Hutter, Yashraj Narang, Soha Pouya, Shiwei Sheng, Yuke Zhu, Miles Macklin, Adam Moravanszky, Philipp Reist, Yunrong Guo, David Hoeller, and Gavriel State. Isaac Lab - A GPU-Accelerated Simulation Framework for Multi-Modal Robot Learning. *arXiv preprint arXiv:2511.04831*, 2025.
- [23] Takuzumi Nishio, Moju Zhao, Kei Okada, and Masayuki Inaba. Design, control, and motion planning for a root-perching rotor-distributed manipulator. *IEEE Transactions on Robotics*, 40:660–676, 2023.
- [24] NVIDIA. Isaac Sim.
- [25] Lerrel Pinto, Marcin Andrychowicz, Peter Welinder, Wojciech Zaremba, and Pieter Abbeel. Asymmetric actor critic for image-based robot learning. In *Robotics: Science and Systems (RSS)*, 2018.
- [26] Aravind Rajeswaran, Vikash Kumar, Abhishek Gupta, Giulia Vezzani, John Schulman, Emanuel Todorov, and Sergey Levine. Learning complex dexterous manipulation with deep reinforcement learning and demonstrations. *arXiv preprint arXiv:1709.10087*, 2017.
- [27] Nikita Rudin, David Hoeller, Marko Bjelonic, and Marco Hutter. Advanced skills by learning locomotion and local navigation end-to-end. In *2022 IEEE/RSJ International Conference on Intelligent Robots and Systems (IROS)*, pages 2497–2503. IEEE, 2022.
- [28] John Schulman, Filip Wolski, Prafulla Dhariwal, Alec Radford, and Oleg Klimov. Proximal policy optimization algorithms. *arXiv preprint arXiv:1707.06347*, 2017.
- [29] Clemens Schwarke, Mayank Mittal, Nikita Rudin, David Hoeller, and Marco Hutter. Rsl-rl: A learning library for robotics research. *arXiv preprint arXiv:2509.10771*, 2025.
- [30] David Shawky, Chao Yao, and Klaus Janschek. Nonlinear model predictive control for trajectory tracking of a hexarotor with actively tilttable propellers. In *2021 7th International conference on automation, robotics and applications (ICARA)*, pages 128–134. IEEE, 2021.
- [31] Eric Sihite, Arash Kalantari, Reza Nemovi, Alireza Ramezani, and Morteza Gharib. Multi-modal mobility morphobot (m4) with appendage repurposing for locomotion plasticity enhancement. *Nature communications*, 14(1):3323, 2023.
- [32] Yunlong Song, Angel Romero, Matthias Müller, Vladlen Koltun, and Davide Scaramuzza. Reaching the limit in autonomous racing: Optimal control versus reinforcement learning. *Science Robotics*, 8(82):eadg1462, 2023.
- [33] Yao Su, Lecheng Ruan, Pengkang Yu, Chen-Huan Pi, Matthew J Gerber, and Tsu-Chin Tsao. A fast and efficient attitude control algorithm of a tilt-rotor aerial platform using inputs redundancies. *IEEE Robotics and Automation Letters*, 7(2):1214–1221, 2021.
- [34] Yao Su, Pengkang Yu, Matthew J Gerber, Lecheng Ruan, and Tsu-Chin Tsao. Fault-tolerant control of an over-actuated uav platform built on quadcopters and passive hinges. *IEEE/ASME Transactions on Mechatronics*, 29(1):602–613, 2023.
- [35] Junichiro Sugihara, Moju Zhao, Takuzumi Nishio, Kei Okada, and Masayuki Inaba. Beetle—self-reconfigurable aerial robot: Design, control and experimental validation. *IEEE/ASME Transactions on Mechatronics*, 2024.
- [36] Jie Tan, Tingnan Zhang, Erwin Coumans, Atil Iscen, Yunfei Bai, Danijar Hafner, Steven Bohez, and Vincent Vanhoucke. Sim-to-real: Learning agile locomotion for quadruped robots. *arXiv preprint arXiv:1804.10332*, 2018.
- [37] Robin Verschueren, Gianluca Frison, Dimitris Kouzoupis, Jonathan Frey, Niels van Duijkeren, Andrea Zanelli, Branimir Novoselnik, Thivaharan Albin, Rien Quirynen, and Moritz Diehl. acados—a modular open-source framework for fast embedded optimal control. *Mathematical Programming Computation*, 14(1):147–183, 2022.
- [38] Huayi Wang, Zirui Wang, Junli Ren, Qingwei Ben, Tao Huang, Weinan Zhang, and Jiangmiao Pang. Beamdojo: Learning agile humanoid locomotion on sparse footholds. In *Robotics: Science and Systems (RSS)*, 2025.
- [39] Hao Xu, Yichen Zhang, Boyu Zhou, Luqi Wang, Xinjie Yao, Guotao Meng, and Shaojie Shen. Omni-swarm: A decentralized omnidirectional visual-inertial-uwB state estimation system for aerial swarms. *Ieee transactions on robotics*, 38(6):3374–3394, 2022.
- [40] Shaohang Xu, Lijun Zhu, Hai-Tao Zhang, and Chin Pang Ho. Robust convex model predictive control for quadruped locomotion under uncertainties. *IEEE Transactions on Robotics*, 39(6):4837–4854, 2023.
- [41] Chenyu Yang, Guo Ning Sue, Zhongyu Li, Lizhi Yang, Haotian Shen, Yufeng Chi, Akshara Rai, Jun Zeng, and Koushil Sreenath. Collaborative navigation and manipulation of a cable-towed load by multiple quadrupedal robots. *IEEE Robotics and Automation Letters*, 7(4):10041–10048, 2022.
- [42] Dingqi Zhang, Antonio Loquercio, Xiangyu Wu, Ashish Kumar, Jitendra Malik, and Mark W Mueller. Learning a single near-hover position controller for vastly different quadcopters. In *2023 IEEE International Conference on Robotics and Automation (ICRA)*, pages 1263–1269. IEEE, 2023.
- [43] Moju Zhao, Tomoki Anzai, and Takuzumi Nishio. Design, modeling, and control of a quadruped robot spidar:

Spherically vectorable and distributed rotors assisted air-ground quadruped robot. *IEEE Robotics and Automation Letters*, 8(7):3923–3930, 2023.

- [44] Moju Zhao, Kei Okada, and Masayuki Inaba. Versatile articulated aerial robot dragon: Aerial manipulation and grasping by vectorable thrust control. *The International Journal of Robotics Research*, 42(4-5):214–248, 2023.
- [45] Xin Zhou, Xiangyong Wen, Zhepei Wang, Yuman Gao, Haojia Li, Qianhao Wang, Tiankai Yang, Haojian Lu, Yanjun Cao, Chao Xu, et al. Swarm of micro flying robots in the wild. *Science Robotics*, 7(66):eabm5954, 2022.
- [46] Yi Zhou, Connelly Barnes, Jingwan Lu, Jimei Yang, and Hao Li. On the continuity of rotation representations in neural networks. In *Computer Vision and Pattern Recognition Conference (CVPR)*, 2019.